Simulation of Residual Stresses and Distortions in a 17-4 PH Part Produced by Laser Powder Bed Fusion

D Galles,[1] C Chin,[2] V Oancea[2]

[1]Weapons and Materials Research Directorate, Army Research Laboratory, Aberdeen Proving Grounds, MD 21005, USA

[2]Simulia Headquarters, Johnston, RI 02911, USA

Abstract: *Mitigation of residual stresses and distortions in additive manufactured parts is of great interest to industry. In this study, an arch-shaped geometry is simulated using the general purpose finite element code Abaqus® in order to predict stresses and distortions for a laser powder bed fusion (LPBF) manufacturing process. A sequential thermal-mechanical coupling is adopted, in which temperatures are predicted first and then used as inputs in the static stress analysis. The printed part is modeled as an elasto-visco-plastic material, whose parameters are estimated using high temperature mechanical measurements from the literature. The layer-by-layer printing process is simulated by progressive element activation in conjunction with a moving heat source. After removal from the build plate, the simulations predict an outward distortion of the arch legs which qualitatively matches experimental observations of a similar geometry.*

Keywords: *additive manufacturing, laser powder bed fusion, 17-4 PH stainless steel, Abaqus, finite element, residual stresses.*

1. Introduction

Laser powder bed fusion (LPBF) is an additive manufacturing technique that produces a 3D metal part in a layer-by-layer fashion. For each new layer, a coating of metal powder is applied over the previous layer and then, utilizing a laser, selectively melted based on a CAD file. The laser power is such that the sub-layer also experiences melting, causing each new layer to be fused to the previous one. After the final layer is produced, the un-melted powder is shaken off, leaving behind the printed part.

LPBF has several advantages over traditional manufacturing processes. In many cases, a complex geometry can be produced as a single part when utilizing LPBF, whereas traditional processes require the assembly of many parts to produce the same geometry. With the ability to produce such complex parts, LPBF can also be coupled with topology optimization to build parts that maximize performance in regards to strength-to-weight ratio, heat transfer, fluid flow, etc. In addition, the small size (10s of microns) of the powder metal particles and laser beam diameter enable the production of parts with extremely fine features. Also, LPBF produces near-net shaped parts that require minimal post-manufacturing processes (i.e., welding, machining, grinding).

Unfortunately, the highly focused laser beam subjects the part to localized rapid heating and cooling, generating large temperature gradients and inducing considerable stresses. This may lead to undesirable results such as large plastic strains or residual stresses and diminish the part life.

The purpose of this study is to predict distortions and residual stresses in a 17-4 PH stainless steel produced by a laser powder bed fusion manufacturing process. For the simulations, variations of a simple arch geometry are used, as well as two scanning strategies to predict different levels of stresses. A sequential thermal-mechanical coupling is utilized, in which temperatures are predicted first and then used as inputs for a static stress analysis. Both analyses are performed using the general purpose finite element code Abaqus®. The temperature-dependent properties used for the heat transfer and stress analyses are estimated using thermodynamic software and high temperature mechanical data from the literature, respectively. The finite element predictions demonstrate the capability of the Abaqus® additive manufacturing module.

2. Simulation Model Setup

For the simulations, three variations of a simple arch design were chosen, whose geometries are shown in Figure 1. The outer dimensions of each arch is identical (30 mm length × 21.32 mm height × 5 mm width). The main difference between the arches is that their top length (see Figure 1(c)) varies (7.5 mm, 15 mm, and 30 mm for arches 1, 2, and 3, respectively). A 1 mm radius was used to reduce stress concentrations on the underside of the arch, where the legs converge. The portion of the arches above the legs is denoted the arch "body", which is 5 mm in height for all arches.

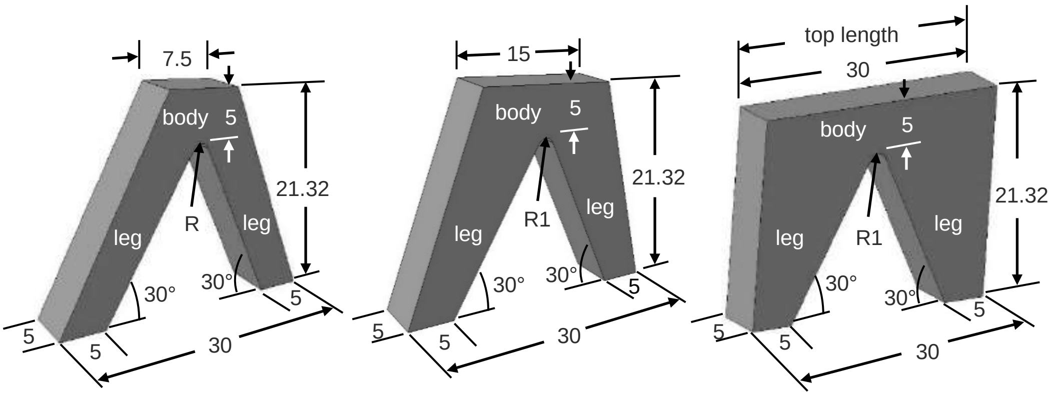

(a) Arch 1 (b) Arch 2 (c) Arch 3

Figure 1. Arch geometries. Dimensions are in mm.

Two scan strategies (termed “0 degree” and “90 degree”) were selected for the simulations and are shown in Figure 2. The simulation design was motivated by the work from Kruth et al. [1], who found that the tensile stresses in the printed part increase with an increasing scan vector. For example, using the 0 degree scan strategy for arch 3 (scan vector = 30 mm) can expected to generate the largest tensile stress along the length of the body, whereas the same scan strategy for arch 1 (maximum scan vector = 7.5 mm) should generate the smallest tensile stresses. Conversely, using the 90 degree scan strategy for arch 3 can be expected to generate lower tensile stresses in the lengthwise direction than the 0 degree strategy. Thus, four cases were chosen: 1) arch 1 with a 0 degree scan strategy, 2) arch 2 with a 0 degree scan strategy, 3) arch 3 with a 0 degree scan strategy, and 4) arch 3 with a 90 degree scan strategy. These cases are summarized in Table 1.

For each case, a sequential thermo-mechanical coupling was utilized, in which temperatures were predicted first and then used an inputs in the stress analysis. Simulation models for each analysis are shown in Figure 3. For the heat transfer analysis (Figure 3(a)), the powder bed was included to simulate heat conduction from the part into the powder bed. The height of the powder bed (21.32 mm) was the same as the part height. For the stress analysis, the powder bed was not included, as the metal powder can be expected to have minimal impact on the stresses in the arches. Build plate dimensions are shown in Figure 3(b). For the meshes, linear brick elements (DC3D8) were used for the arch in the heat transfer analysis, whereas linear tetrahedral elements (DC3C4) were used for the build plate and powder bed. Figure 4 shows the mesh for the stress analysis, in which linear brick elements (C3D8) were utilized for both the arch and build plate. Characteristic lengths for the arch elements were approximately 0.5 mm. Roughly speaking, approximately 100,000 nodes and 400,000 elements were used to run the heat transfer analysis, whereas 70,000 nodes as 60,000 were used in the stress analysis. The models shown in Figure 3 comprise a single part containing different sections that define the material properties for the arch, powder bed, and build plate. Thus, no contact resistance was considered between the arch and powder bed.

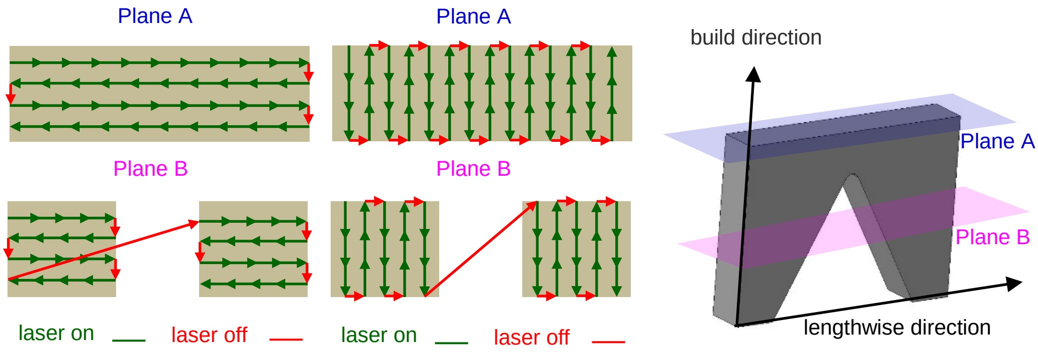

(a) 0 degrees **(b) 90 degrees** **(c) Slice Planes**

Figure 2. Schematics of the 0 (a) and 90 (b) degree scan strategies are depicted on the slice planes shown in (c).

Table 1. Simulation cases.

Case	Arch	Scan Strategy
1	1	0 degree
2	2	0 degree
3	3	0 degree
4	4	90 degree

Two event series (roller and laser power) were constructed to govern 1) the application of powder layers, and 2) heat input from the laser as a function of position and time. Progressive element activation was utilized to simulate building of the part in a layer-by-layer fashion. The time to apply each powder layer was estimated to be 8 s. For the heat transfer analysis, the powder bed and arch element activations coincided with the roller event series, whereas only the arch was activated for the stress simulation (since the powder bed was not included in the stress analysis). For the laser power event series, the heat input data was extracted from the software package Phenix Processing®, which is used to build the sliced CAD files for 3D Systems® printing machines. For the simulations, a single time increment was used for both the layer application (8 s) and for the duration of the moving heat source for each layer, which varied between 1 and 2.5 s.

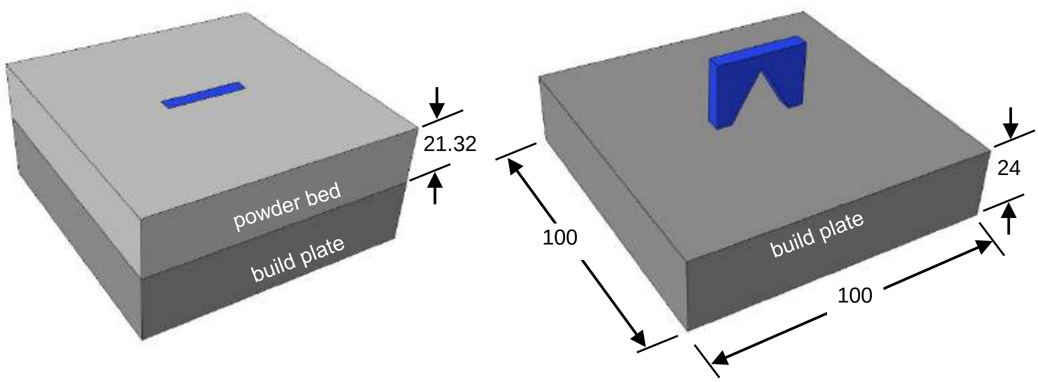

(a) Heat Transfer Model **(b) Stress Model**

Figure 3. Abaqus models for the heat transfer (a) and stress (b) simulations for arch 3. The powder bed was not included in the stress simulation. Dimensions

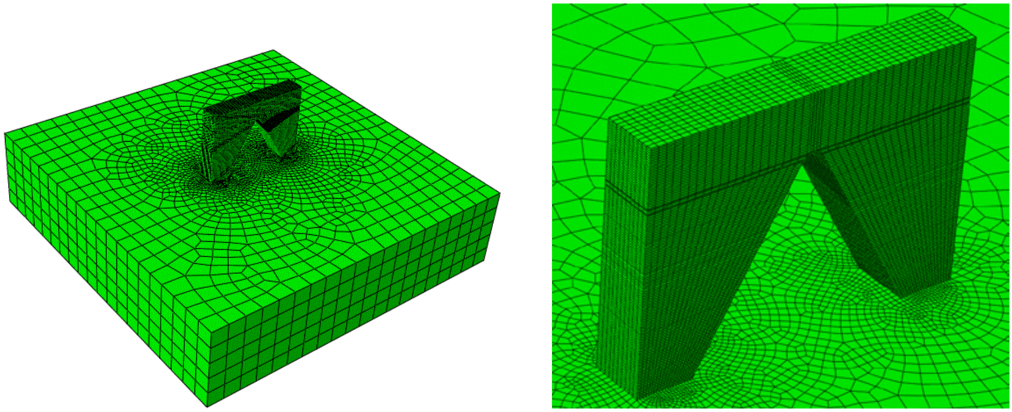

(a) Complete mesh **(b) Arch mesh**

Figure 4. The Abaqus mesh for stress simulations utilized linear brick elements (C3D8) for the aches and build plate.

3. Heat Transfer Simulations

For the heat transfer analysis, thermophysical properties for the arch and build plate were determined from the thermodynamic software package IDS [2] using the 17-4 PH stainless steel chemistry shown in Table 2. The calculated properties are shown in Figure 5. The effects of latent heat of solidification and the solid state phase transformation were combined with the specific heat by taking the discreet temperature derivative of the predicted enthalpy and shown as the effective specific heat in Figure 5(b). The latent heat effects of solidification and solid state phase transformation can be seen as spikes in the curve at the liquidus temperature (T_{liq}) and 610°C, respectively. For other heat transfer parameters, the emissivity was set to 0.25 and the absorption coefficient was set to 0.45.

For the powder bed, the study of Moser et al. [3] was used to estimate the effective thermal conductivity of the powder bed as a function of temperature, particle size, solid conductivity, and atmospheric gas conductivity (nitrogen). The powder bed density was estimated by measuring the room temperature value and extrapolating the room temperature density ratio ($\rho_{solid}/\rho_{powder\ bed}$) to high temperatures. The effective specific heat for the powder bed was set to the value of the solid material.

Results for the heat transfer simulation are shown in Figure 6 at various build heights. These images show the maximum temperature in the layer, which occurs immediately after the laser is turned off. In general, the predicted temperatures range between room temperature and 300°C, with the exception of the 16.32 mm height, for which temperatures can be seen approaching

Table 2. 17-4 PH stainless steel chemistry used to determine thermophysical properties.

%Cr	%Ni	%Mn	%Si	%Nb	%Cu	%P	%C	%S	%Fe
17.5	5	1	1	0.15	5	0.04	0.07	0.03	70.21

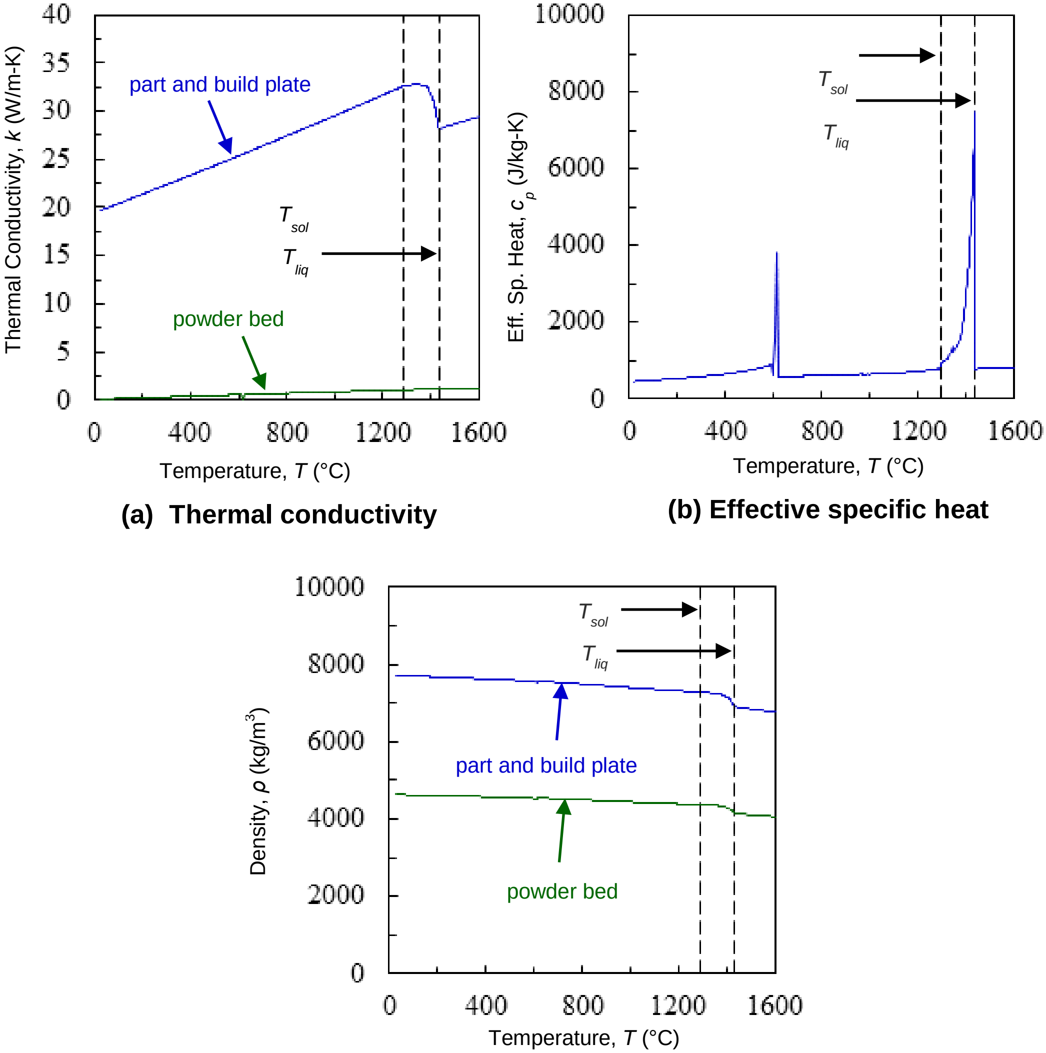

(a) Thermal conductivity

(b) Effective specific heat

(c) Density

Figure 5. Temperature dependent thermophysical properties were estimated with IDS [ref] software using the chemistry shown in Table 1. The effective specific heat includes latent heat effects for solidification and the solid state phase transformation.

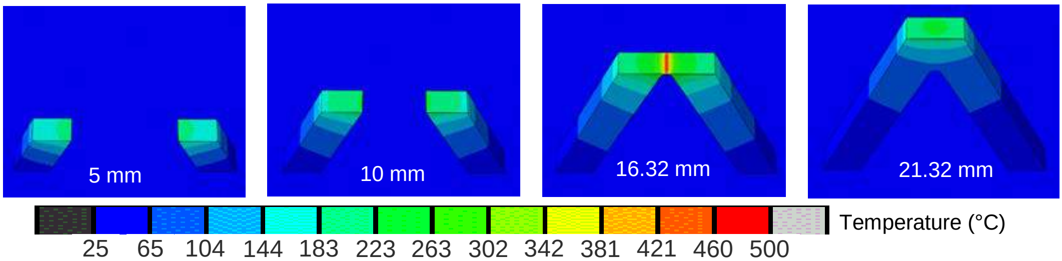

(a) Arch 1 horizontal laser scan strategy

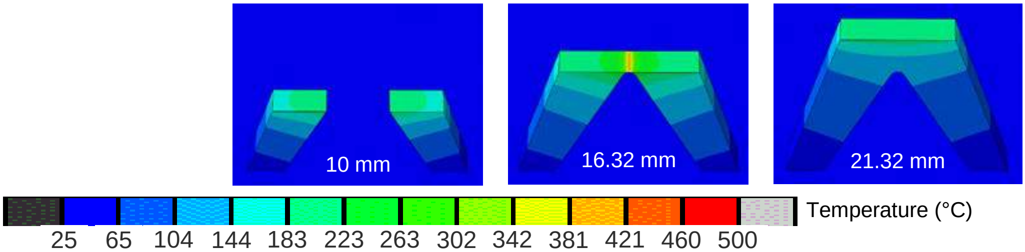

(b) Arch 2 horizontal laser scan strategy

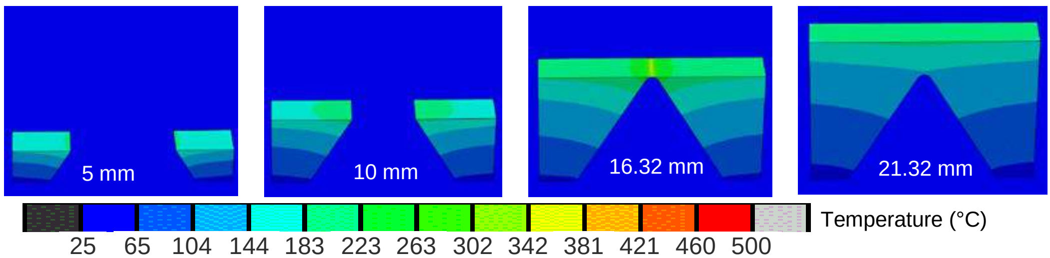

(c) Arch 3, 0 degree laser scan strategy

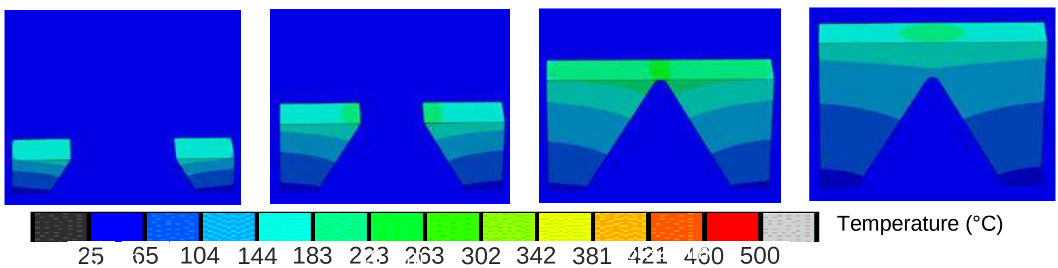

(d) Arch 3, 90 degree laser scan strategy

Figure 6. Predicted temperatures at various build heights for simulations using a single time increment during melting for each layer.

500°C. These higher temperatures are due to a lack of solid material to conduct heat away immediately when a bridge between the two legs is formed. The relatively low temperature predictions are due mainly to the large increments taken while the laser is on. Larger predicted temperatures can be expected for smaller time increments. A parametric study will be performed to investigate the effect of the time increment on maximum predicted temperatures. Also, the large increments prevented any discernible difference to be seen between the 0 and 90 degree scan strategies, i.e., no scan vectors could be seen.

Figure 7 shows an example (for arch 1) of the change in predicted temperatures immediately before the laser is activated and after the laser is deactivated. This illustrates the predicted cooling that occurs while a new layer of powder is applied. From the figure, it can be seen that the arch cools from a maximum temperature of 500°C at a height of 16.32 mm to less than 150°C after the roller has finished applying a new layer. Again, due to the large time increment, the actual temperature fluctuations in a real part are expected to be much larger. Nevertheless, this demonstrates the thermal cycling that is associated with laser powder bed fusion. Such variations can be expected to have a considerable effect on the microstructure.

(a) Prior to laser activation **(b) After laser deactivation**

Figure 7. Predicted temperatures for arch 1 immediately before laser activation (a) and after laser deactivation (b).

4. Static Stress Simulations

The stress model solves for the evolution of stresses and displacements in the arch and build plate. The small strain assumption is adopted for the present study. Assuming negligible inertial effects, body forces, and momentum transport between the solid and liquid during solidification, the solid momentum equation is reduced to a zero divergence of the stress tensor ($\boldsymbol{\sigma}$), i.e., $\nabla \cdot \boldsymbol{\sigma} = 0$. The strain tensor ($\boldsymbol{\varepsilon}$) is additively decomposed into its elastic ($\boldsymbol{\varepsilon}_e$), inelastic ($\boldsymbol{\varepsilon}_{in}$), and thermal ($\boldsymbol{\varepsilon}_{th}$) components.

The build plated was modeled as an isotropic, homogeneous elastic material, as stresses in the arch are unlikely to cause yielding in the build plate. The constitutive law for the arches considers rate, hardening, and temperature affects and is modeled as a pressure-dependent material during solidification. Below the solidus temperature, the model reduces to a standard elasto-visco-plastic constitutive law. The model is adopted from Monroe and coworkers [4,5] and is reviewed by Galles and Beckermann [6].

For the elastic properties, Young's modulus was taken from Koric and Thomas [7] and is shown in Figure 8(a). A constant Poisson's ratio of 0.3 was used.

Thermal strains were calculated using the relation $\boldsymbol{\varepsilon}_{th} = \alpha_{tot}(T - T_{th})\mathbf{1}$, where T is the temperature, T_{th} is the temperature at the onset of thermal contraction, $\mathbf{1}$ is the 2nd order identity tensor. The total linear thermal expansion coefficient, α_{tot}, was determined from the density (calculated by IDS) and is shown in Figure 8(b).

Upon yielding, the stress-strain relation for the arches are governed by

$$\sigma_{dy} = \sigma_0 \left(1 + \frac{\varepsilon_{pl}}{\varepsilon_0}\right)^n \left(1 + \frac{\dot{\varepsilon}_{pl}}{\dot{\varepsilon}_0}\right)^m \qquad [1]$$

where σ_{dy} is the dynamic yield stress, σ_0 is the initial yield stress, ε_{pl} is the equivalent plastic strain, ε_0 is the reference strain, n is the hardening exponent, $\dot{\varepsilon}_{pl}$ is the equivalent plastic strain rate, $\dot{\varepsilon}_0$ is the reference strain rate, and m is the strain rate sensitivity exponent. These parameters

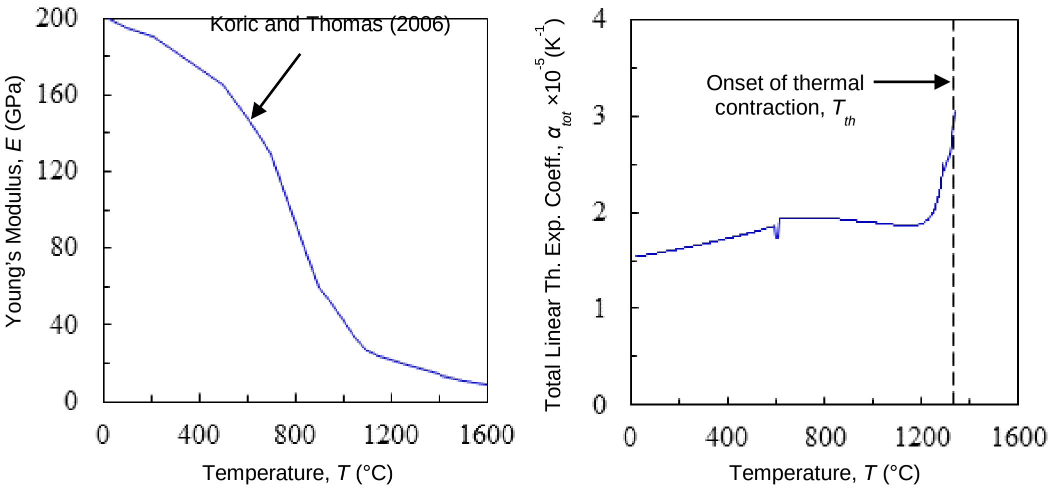

(a) Young's Modulus

(b) Total Linear Thermal Expansion Coefficient

Figure 8. Young's Modulus (a) was taken from Koric and Thomas [7]. The total linear thermal expansion coefficient (b) was calculated from the temperature dependent density predicted by IDS [2].

were estimated from the high temperature mechanical tests performed on reheated samples of 17-4 PH stainless steel between for temperatures between 950°C and 1150°C and strain rates ranging from 10^{-3} to 1 s^{-1} [8] using a Levenberg-Marquardt nonlinear parameter estimation algorithm. The complete details are described elsewhere [6]. The estimated parameters were then extrapolated to include the range from the liquidus temperature (1435°C) down to the solid state phase transformation at 610°C and are plotted as functions of temperature in Figure 9. Below 610°C, the material was assumed to be rate-independent (i.e., *m* was set to zero), causing the rate-dependent term to vanish from Equation 1. The remaining parameters (σ_0 , n, ε_0) were determined from a room temperature tensile test. Between room temperature and 610°C, values were linearly interpolated.

In order to evaluate the fit, Equation 1 was used to predict the stresses using the mechanical test data from which the parameters were estimated. Figure 10 shows a comparison between the measured and predicted stresses using the experimental viscoplastic strains and strain rates. In general, the model predicts the material response well. At lower strain rates, however, the model slightly under-predicts the stress response. Further tuning of the estimated parameters may needed to achieve better agreement. As a first estimate, though, the estimated parameters are reasonable.

Stress and equivalent plastic strain contours are shown for all simulations in Figure 11. Distortions are magnified 5x. Contours are shown after the part has been built but before removal from the build plate. Large von Mises stresses (> 500 MPa) are predicted throughout the arches, with localized values near the top of the overhang area greater than 1000 MPa. Normal stresses in the lengthwise direction (see Figure 2(c)) are predominantly tensile with most regions also over 500 MPa. Larger tensile stress variations are seen in the build direction, as large stress concentrations are predicted near the outsides of the legs and along the build height. The predicted equivalent plastic strains are also large, with values mostly exceeding 0.2 throughout the arches.

Using *Model Change, the arches were removed from the build plate after the build had completed. Some amount of stress relaxation can be expected from this procedure depending on the level of residual stresses in the arches. Figure 12 shows an outward “spring back” of approximately 0.15 mm for the case 4 (arch 3, 0 degree) legs after removal. This prediction is in line with the experimental observations by Kruth et al. [1]. The spring back for all arches is shown in Figure 13. The arch 1 simulation predicted the largest spring back, whereas arch 3 predicted the smallest amount. These results are unexpected. The longer scan vectors used in arch 3 were expected to produce the largest tensile stresses in the body of the arch, which would in turn generate the largest amount of spring back. Possibly, the extra material in arch 3 provided restraint and minimized the amount of pushout of the legs. The large tensile stresses seen in the build direction near the outsides of the legs (see Figure 11(c)) may have caused the larger spring back that was predicted for arch 1.

Negligible differences can be seen between the 0 and 90 degree scan strategies for arch 3. Since only 1 increment was used during melting for each layer, the scan directions were not considered by the simulation. Thus, the similarity in the results for the 0 and 90 degree strategies is not unexpected.

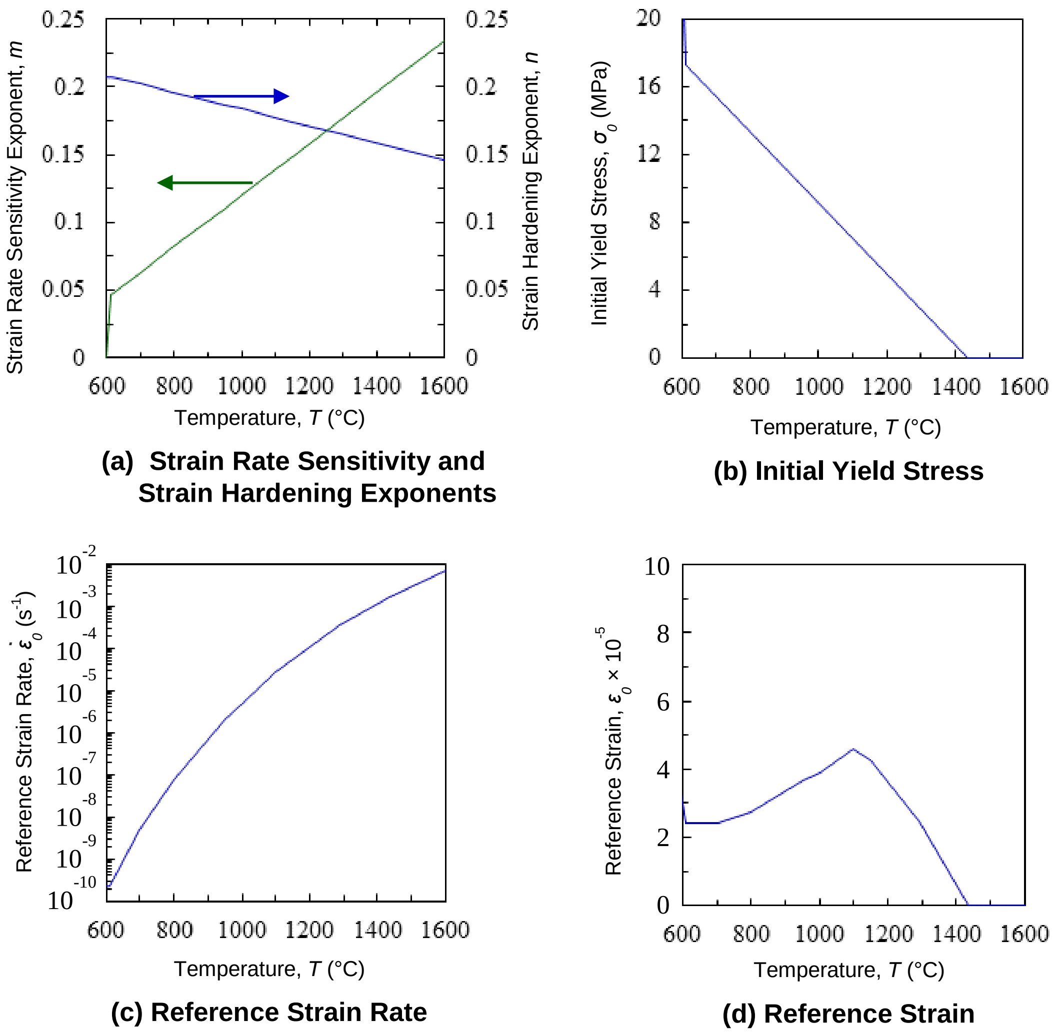

Figure 9. Estimations for the viscoplastic model parameters used in Equation 1.

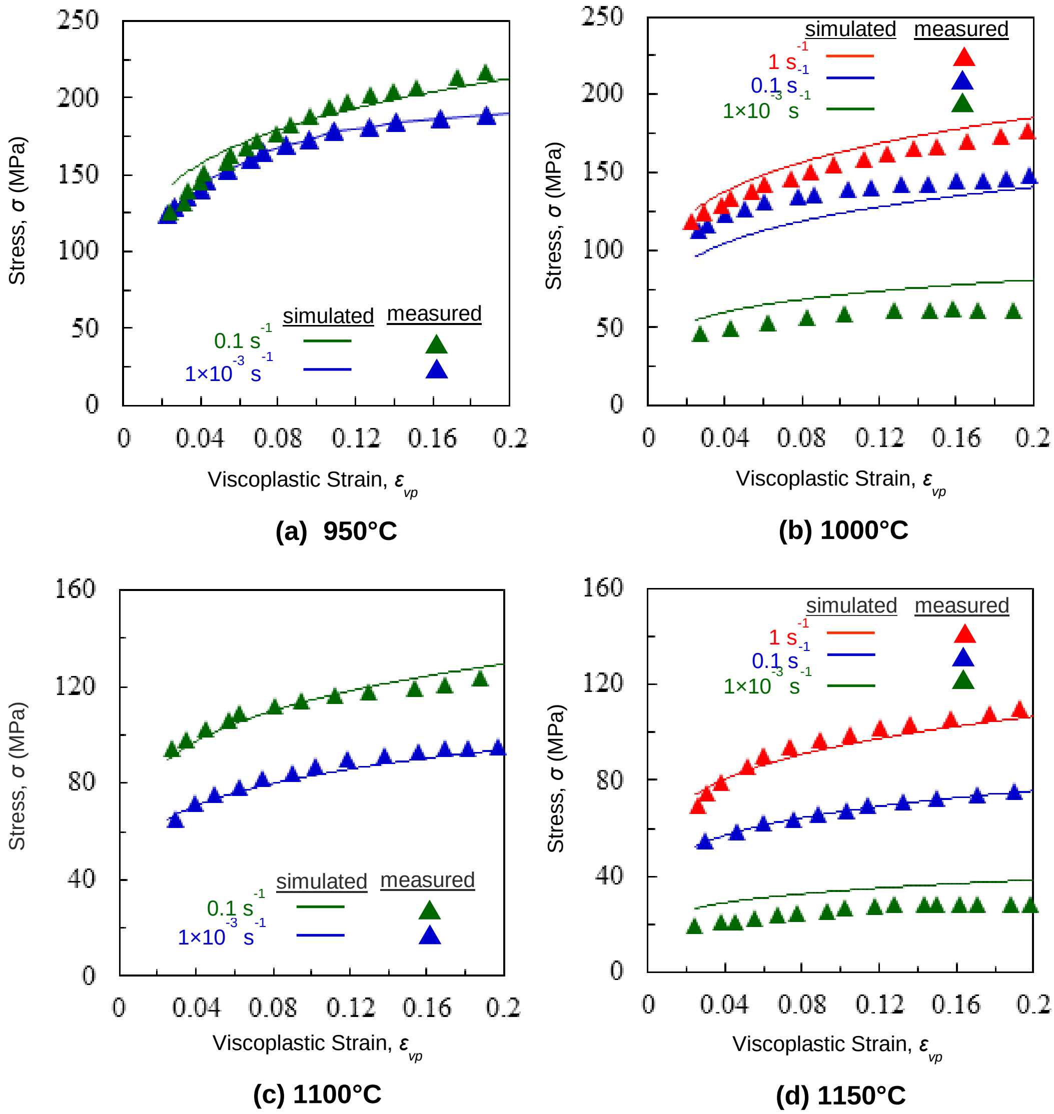

Figure 10. Comparison between measured and predicted stresses for 17-4 PH stainless steel at temperatures ranging from 950°C to 1150°C and strain rates from $1{\times}10^{-3}$ to 1 s^{-1}.

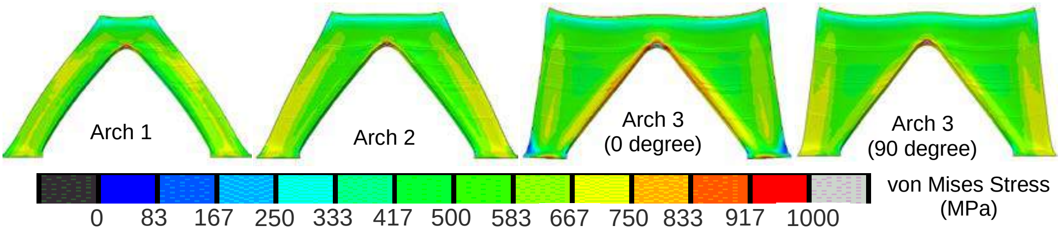

(a) von Mises stress

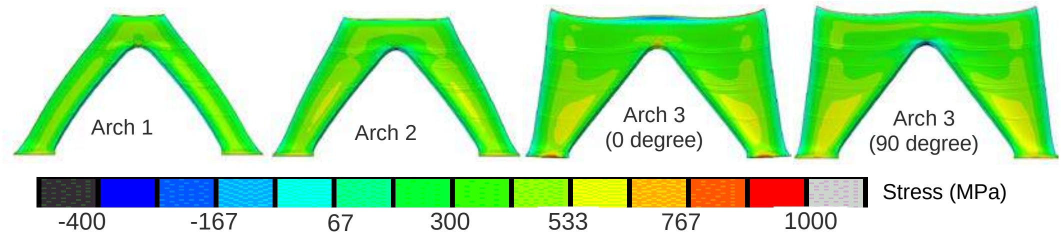

(b) Normal stresses for lengthwise direction

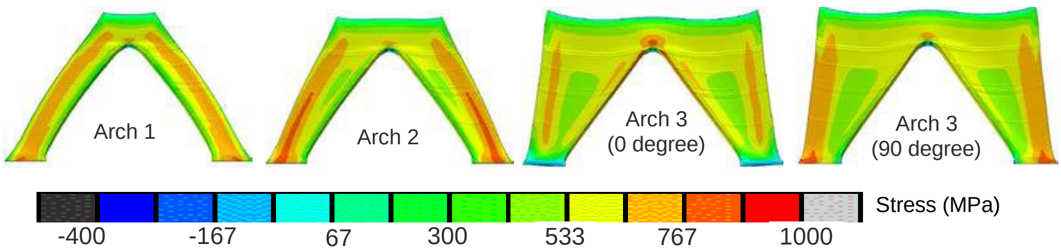

(c) Normal stresses for build direction

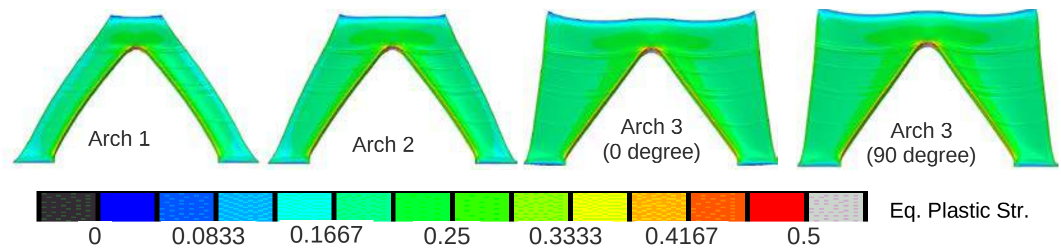

(d) Equivalent plastic strains

Figure 11. Predicted stresses and equivalent plastic strains.

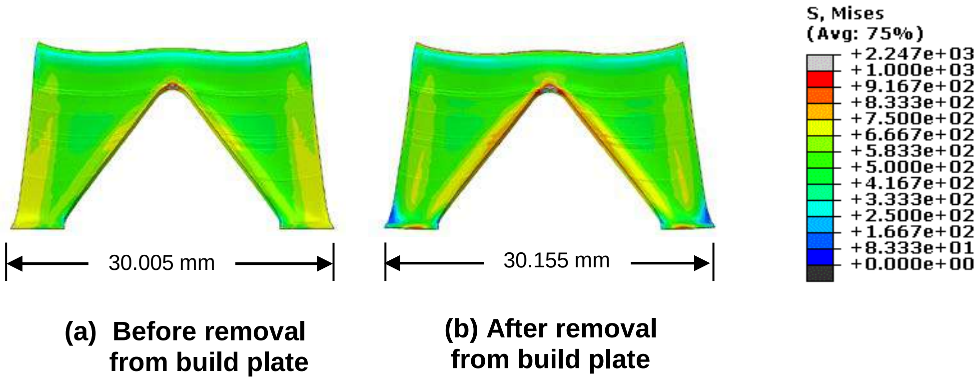

Figure 12. Outer distance between arch 3 legs for 0 degree scan strategy before (a) and after (b) removal from the build plate. Von mises stress contours with units of MPa are shown.

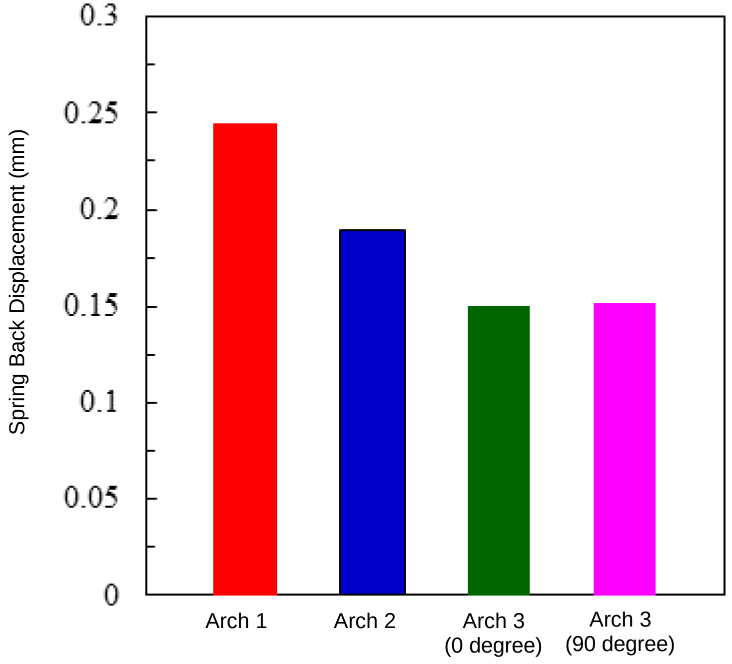

Figure 13. Spring back displacement after build plate removal for all arches. The positive values represent an outward deflection of the arch legs.

5. Conclusions and Future Work

In this study, a laser powder bed fusion process was simulated in Abaqus® to predict stresses and distortions in a 3D-printed 17-4 PH stainless steel part. Three variations of an arch and two different scan strategies were utilized for the purpose of predicting different amounts of stress and associated distortions. Progressive element activation and a moving heat source were used to simulate the process. Due to the coarse time increments, maximum temperatures of only 500°C were predicted in the arches, compared to a melting temperature of nearly 1300°C. In spite of this, the predicted behavior of the arches after removal from the build plate followed the observed trends from the literature.

For future work, validation experiments will be performed, at which time quantitative comparisons can be made to determine the accuracy of the computational model. In addition, experiments are planned to measure the effective thermal conductivity in the powder bed. This experimental work will be crucial for model validation as well as guide future experimental and simulation design.

6. References

1. Kruth J.P., Deckers J., Yasa E., and Wauthle, R., "Assessing and Comparing Influencing Factors of Residual Stresses in Selective Laser Melting Using a Novel Analysis Method," *Proc IMechE Part B: J Engineering Manufacture*. vol 226, no. 6, 2012, pp. 980-91 .
2. Miettinen J., "Calculation of Solidification-related Thermophysical Properties for Steels," *Metall Mat Trans B*, vol. 28, 1997, pp. 281-97.
3. Moser D., Pannala S., and Murthy J., "Computation of Effective Thermal Conductivity of Powders for Selective Laser Sintering Simulations," *J Heat Transfer*, vol. 138, 2016.
4. Monroe C., Ph.D. Thesis, University of Iowa, Iowa City, IA, 2009.
5. Pokorny M., Monroe C., Beckermann C., Bichler L., and Ravindran C., "Prediction of Hot Tear Formation in a Magnesium Alloy Permanent Mold Casting," *Int J Metalcasting*, vol. 2, no. 4, 2008, pp. 41-53.
6. Galles D. and Beckermann C., "In Situ Measurement and Prediction of Stresses and Strains During Casting of Steel," *Metall and Mat Trans A*, vol. 47, no. 2, 2016, pp. 811-29.
7. Koric S. and Thomas B.G., "Efficient Thermo-mechanical Model for Solidification Processes," *Int J Numer Methods Eng*, vol. 66, 2006, pp. 1955-89.
8. Mirzadeh H. and Najafizadeh A., "Flow Stress Prediction at Hot Working Conditions," *Mat Sci Eng A*, vol. 527, 2010, pp. 1160-4.